Modeling the Phase-Change Cooling of Molten Slag Granule: An Appraisal

Yuhao Xiang[1,2], Junjun Wu[1,2]*, Yiwen Lv[1,2], Hong Wang[1,2], Xun Zhu[1,2]*, Qiang Liao[1,2]

1 Key Laboratory of Low-grade Energy Utilization Technologies and Systems, Chongqing University, Ministry of Education, Chongqing 400044, China

2 Institute of Engineering Thermophysics, School of Energy and Power Engineering, Chongqing University, Chongqing 400044, China
(*Corresponding Authors: jjwu@cqu.edu.cn (J. Wu); zhuxun@cqu.edu.cn (X. Zhu))

ABSTRACT

An accurate understanding of slag cooling characteristics is essential for efficient slag heat recovery. Herein, we established multiple cases including different assumptions, such as dimensions, boundary conditions, width ratios, radiation models, and turbulence models to quantify the extent of error associated with these assumptions. An area-weight angle sampling method was adopted to evaluate the accuracy of assumptions. The results reveal the significant error attributed to dimensions and radiation, with RMSE and MAPE of 235.14 K and 41.30% for the 2D planar model, and 198.60 K and 25.66% for the model without radiation. Notably, when the width ratio exceeds 4, the influence of boundary conditions on cooling characteristics becomes negligible. This present work provides a benchmark model to quantify the error of assumptions and thus enables more accurate yet efficient modeling for phase-change cooling for molten slag at ultrahigh temperatures.

Keywords: waste heat recovery, droplet cooling, phase change, dry slag granulation

NONMENCLATURE

Abbreviations	
BFS	Blast furnace slag
ISI	Iron and steel industry
MAPE	Mean absolute percentage error
RMSE	Root mean squared error
WR	Width ratio ($\mathrm{WR} = w/r$)
S2S	Surface-to-surface model
2D	Two dimensional
3D	Three dimensional

Symbols	
A_{mush}	Mushy zone constant (kg·m^{-3}·s^{-1})
c_p	Specific heat (J·kg^{-1}·K^{-1})
f_l	Liquid fraction
F	View factor
g	Gravity (m·s^{-2})
H	Enthalpy (J·kg^{-1})
k	Turbulence kinetic energy (m^2·s^{-2})
L	Latent heat (J·kg^{-1})
p	Pressure (Pa)
r	Radius (m)
S_v	Source term of velocity (kg·m^{-2}·s^{-2})
S_R	Source term of radiation (J·m^{-3}·s^{-1})
T	Temperature (K)
v	Velocity (m·s^{-1})
w	Width of computational domain (m)
ε_r	Emissivity
λ	Thermal conductivity (W·m^{-1}·K^{-1})
μ	Viscosity (kg·m^{-1}·s^{-1})
ρ	Density (kg·m^{-3})
Φ	Heat flux (W·m^{-2})
ω	Specific dissipation rate (s^{-1})

1. INTRODUCTION

The iron and steel industry (ISI) has long been recognized as one of the largest CO_2 emission sources with a considerable waste heat untapped. Molten slags such as blast furnace slag (BFS) or steel slag at 1500 °C or above hold a large share of the waste heat in ISI. It is very critical to recover the high-temperature waste heat from the molten slags, which thus requires efficient heat transfer between the slag and the coolant (such as air) for further integration with well-established heat utilization technologies [1]. Particularly, high cooling rates are imperative to form the glassy phase slag, which

---

is available for cement clinker production. Therefore, recent techniques like air quenching and centrifugal granulation have emerged to increase the specific surface area, enabling rapid cooling by granulating slag into tiny droplets. These techniques are promising in harvesting the waste heat in molten slags.

The cooling dynamics of the slag particle relate intimately to the heat recovery efficiency and the content of the glassy phase. As a mixture of various oxides, the slag exhibits different liquidus and solidus temperatures. A transitional zone is thus present between the solid outer shell and a liquid inner core of the slag particle during the cooling process; this is the so-called mushy zone in Fig. 1. In the mushy zone, the slag may be re-melt and is thus viscous and adhesive. It is thus highly desirable to form a robust solid shell by fast cooling to prevent slag deformation. Insufficient cooling may lead to agglomeration among the slag particles or slag adhesion on walls, which worsens the heat exchange efficiency, lowers glassy slag formation, and even leads to safety risks.
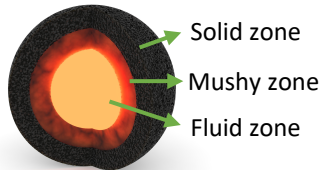

Fig. 1 Internal morphology of the slag particle during solidification

It is crucially important to establish a phase-cooling model for the molten slag particle. Hence, many modeling efforts have been implemented to explore the slag cooling characteristics. Liu et al. [2] developed a one-dimensional (1D) model to analyze the phase-change cooling process of molten BFS particles. The results indicated that the radiation and temperature-dependent thermal conductivity of slag increased the cooling rates significantly. Sun et al. [3] simulated a three-dimensional (3D) slag droplet cooling without airflow, suggesting that temperature differences within the slag might cause crystal formation. Zhu et al. [4] proposed a correlation of the average cooling rate with the crystallization ratio through directional solidification experiments. Gao et al. [5] extended this equation to a two-dimensional (2D) simulation, assuming that the average cooling rate could be replaced by the instantaneous cooling rate. Table 1 lists the typical simplifications and assumptions in previous models. Although valuable insights were provided in the previous efforts, it is altering to find that most previous models adopted rather different simplifications or assumptions, and thus led to inconsistencies in the cooling rates among those models.

Table 1 Typical simplifications and assumptions for the phase-change cooling model of the molten slag particle. Note that the width ratio (WR) represents the ratio of the width w to the slag radius r. i.e., WR = w/r .

Author	Dimension	Boundary	WR ratio	Turbulence	Radiation
Peng et al. [6]	2D	Wall	5	No	No
Zhao et al. [7]	2D	Wall	2	No	DO
Gao et al. [5]	2D	Wall	1+1/r	No	Not mentioned
Qiu et al. [8]	2D axisymmetric	Wall	2	No	No
Wang et al. [9]	3D	Wall	2	k -ε	P1

In this study, we first establish a three-dimensional benchmark model and carry out extensive efforts to systematically evaluate the accuracy of these models with various settings and assumptions. Further, optimal settings were suggested to enable accurate yet efficient modeling for the phase-change cooling of the molten slag.

2. METHODOLOGY

2.1 Model setup

Herein, two assumptions were adopted in this work:
(i) The cooling of slag droplets by flowing air was assumed to maintain a constant relative velocity of slag and air.
(ii) Particle deformation in airflow was neglected based on the report [5], indicating its insignificant deforming magnitude during the slag cooling process.

Fig. 2 displays the 3D and 2D models used in this study. The 3D model is based solely on the basic assumptions, utilizing a significantly large computational domain for high simulation accuracy. Subsequently, the 2D models were used to investigate the effect of the aforementioned assumptions, involving dimension, boundary conditions, width ratio, radiation and turbulence models.
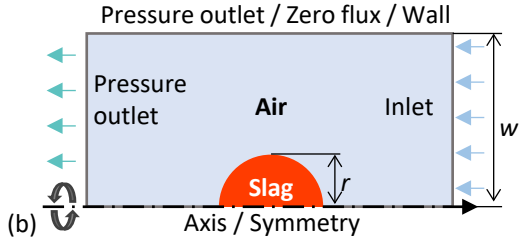

(a)
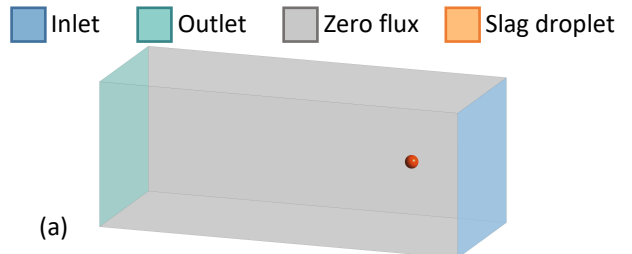
Fig. 2 Schematic diagrams of (a) 3D model and (b) 2D models.

2.2 Equation

Air and slag follow the same equations in their respective computational domains, where the equations are given as follows:

$$\frac{\partial \rho_i}{\partial \tau} + \nabla \cdot (\rho_i \boldsymbol{v}) = 0, \tag{1}$$

$$\frac{\partial \rho_i \boldsymbol{v}}{\partial \tau} + \nabla \cdot (\rho_i \boldsymbol{v}\boldsymbol{v}) = -\nabla p + \nabla \cdot \left[\mu_i \left(\nabla \boldsymbol{v} + \nabla \boldsymbol{v}^T \right) \right] + \rho_i \boldsymbol{g} + \boldsymbol{S}_v, \tag{2}$$

where ρ_i denotes the density of phase i., the symbols p, μ_i, τ, and vector $\boldsymbol{v}$, $\boldsymbol{g}$ represent pressure, viscosity, time, flow velocity, and gravity, respectively. The source term $\boldsymbol{S}_v$ is the resistance term of the solidification model on the flow, which follows the Kozeny - Carman equation as below:

$$\boldsymbol{S}_v = -\frac{(1-f_l)^2}{f_l^3 + \varepsilon} A_{\text{mush}} \boldsymbol{v}, \tag{3}$$

where f_l and A_{mush} are the liquid fraction and the mushy zone constant with the value 10^7. ε is a small number (0.001) that prevents the division by zero.

The SST $k-\omega$ model was used in this study with the equation as follows:

$$\frac{\mathrm{d}\rho k}{\mathrm{d}\tau} + \nabla \cdot (\rho \boldsymbol{v} k) = \nabla \cdot \left[(\mu_l + \frac{\mu_t}{\sigma_{k3}}) \nabla k \right] + P_k - \beta' \rho k \omega, \tag{4}$$

$$\begin{aligned} \frac{\mathrm{d}\rho \omega}{\mathrm{d}\tau} + \nabla \cdot (\rho \boldsymbol{v} \omega) &= \nabla \cdot \left[(\mu_l + \frac{\mu_t}{\sigma_{\omega 3}}) \nabla \omega \right] \\ &+ (1-F_1) 2\rho \frac{\nabla k \nabla \omega}{\sigma_{\omega 2} \omega} + \alpha_3 \frac{\alpha}{k} P_k - \beta_3 \rho \omega^2, \end{aligned} \tag{5}$$

where k and ω are the kinetic energy and the specific dissipation rate. μ_l and μ_t is the molecular and eddy viscosity. α_3, β_3 and β' are constants. σ_{k3} and $\sigma_{\omega 2}$ represent turbulent Prandtl numbers. F_1 is the first blending function.

The energy equation including the surface-to-surface (S2S) radiation model is shown below:

$$\frac{\partial}{\partial \tau}(\rho_i H_i) + \nabla \cdot (\rho_i \boldsymbol{v} H_i) = \nabla \cdot (\lambda_i \nabla T) + S_R, \tag{6}$$

where H_i is the enthalpy of phase i. The slag enthalpy H_{slag} includes latent heat is shown as follows:

$$H_{\text{slag}} = h_{\text{ref}} + \int_{T_{\text{ref}}}^{T} c_{p,\text{slag}} dT + f_l L_{\text{slag}}, \tag{7}$$

The S2S radiation model is added as the source term S_R of the energy equation, which can be expressed as:

$$S_{R,k} = \rho_k \sum_{j=1}^{N} F_{jk} S_{R,j} - \varepsilon_k \sigma T_k^4, \tag{8}$$

where the subscripts j and k represent different surfaces. F_{kj} is the view factor between surface j and surface k.

2.3 Properties of materials

The temperature-dependent properties of air and slag are listed in Table 2.

Table 2 Properties of air and BF slag

Properties		Temperature-dependent value
ρ_{slag}	(kg·m^{-3})	$2750, T \geq 1643$ K $2840, T < 1483$ K $2984.9 - 0.14T$, others
$C_{p,\text{slag}}$	(J·kg^{-1}·K^{-1})	$1302, T \geq 1643$ K $1105, T < 1483$ K $1.23T - 720.9$, others
λ_{slag}	(W·m^{-1}·K^{-1})	[10]
μ_{slag}	(kg·m·s^{-1})	[11]
L_{slag}	(J·kg^{-1})	284000 [4]
$T_{l,\text{slag}}$	(K)	1643 [4]
$T_{s,\text{slag}}$	(K)	1483 [4]
$\varepsilon_{r,\text{slag}}$		0.85
ρ_{air}	(kg·m^{-3})	Ideal gas
$C_{p,\text{air}}$	(J·kg^{-1}·K^{-1})	[10]
λ_{air}	(W·m^{-1}·K^{-1})	[10]
μ_{air}	(kg·m·s^{-1})	[10]

2.4 Simulation strategy and post-processing method

The simulation strategy in this work is to first solve the momentum and continuity equations to obtain the steady-state flow field. Then, the transient solution was calculated by enabling energy-related equations like enthalpy, radiation, and solidification-melting for better convergence. Furthermore, the area-weighted angle sampling method was used to obtain the mean temperature for different angles, as shown in Eq. (9)

$$T_{\tau,\theta} = \frac{\int_0^r 2\pi \sin\theta \, r T_{\tau,\theta} ds}{\int_0^r 2\pi \sin\theta \, r ds} \tag{9}$$

where θ is the angle, r is the droplet radius, and $T_{\tau,\theta,s}$ is the temperature at angle θ. To intuitively

illustrate this method for a specific angle, we provide an example of the averaging area at 45°, as depicted below:
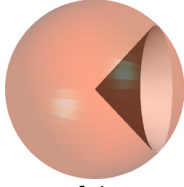

Fig. 3 Schematic diagram of the area-weighted (grey area) angle sampling method with an angle of 45°.

Meanwhile, Root Mean Squared Error (RMSE) and Mean Absolute Percentage Error (MAPE) were used to evaluate the difference between the simplified model and the benchmark model at the same time and angles.

2.5 Grid and model validation

Validations of 3D meshes and 2D meshes with a width ratio of 5 were performed in this study. The 3D model employed grid numbers of 319872, 574950, 804067, and 1664370, while the 2D models had grid numbers of 6928, 12920, 27982, 47750, and 104876. Only a minor error was observed for a grid number of 6928 in the 2D grid. Therefore, the 3D grid number was set at 804067, and the 2D grid number with a width ratio of 5 was chosen at 47750 to avoid potential accuracy loss due to altering the computational domain.

To further validate the simulation's accuracy, the directional solidification experiments of molten alloy by Ferreira et al. [12] were chosen to be simulated. The result shows the maximum temperature error was 2.0%. Hence, it is reasonable to conclude that the model in this work reliably presents the processes of radiation and solidification heat transfer characteristics.

3. RESULTS

3.1 Three-dimensional slag cooling characteristics

To investigate the cooling process of a molten slag droplet in airflow, a 3D simulation was established as a benchmark. The simulation considered an initial temperature of 1773.15 K and a diameter of 4 mm. The cooling air flowed at a rate of 5 m·s^{-1} with an initial temperature of 298.15 K. Fig. 4 illustrates the contour of temperature, cooling rate and liquid fraction. One can observe from Fig. 4 (a) that the cooling air is rapid heating due to convection as it passes over the high-temperature slag droplet. The air's temperature boundary layer thickens gradually along the flow path until separation, and the separation angle increases as the slag cools down. Moreover, there's no significant asymmetry observed. Fig. 4 (b) reveals the windward side of the particles experiencing relatively rapid cooling. During incomplete solidification, the peak of cooling rate

consistently appears at the outer edge of the mushy zone due to the latent heat release. As the slag solidifies completely, this cooling rate peak eventually moves to the leeward side of the center point.
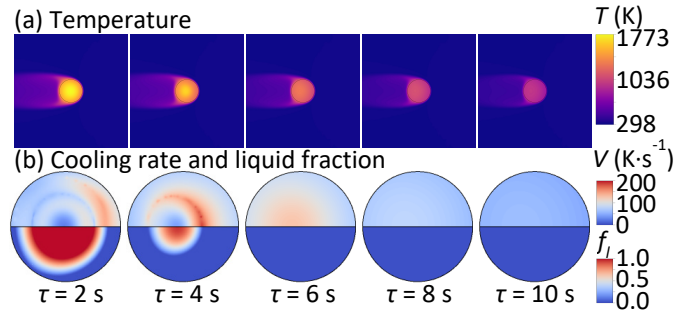

Fig. 4 Contours of (a) temperature and (b) cooling rate (upper part) and liquid fraction (lower part)

Fig. 5 illustrates the distribution of total and radiative heat flux on the slag surface, where the range of circumferential values in each angle are indicated by shadows. Both significant contributions of radiation and convective heat transfer are shown, which dominant radiation occur at the separation point with convection notably decreasing. Moreover, the values at different circumferences tend to remain uniform over time. This axisymmetric result further affirms the usability of the 2D grid.
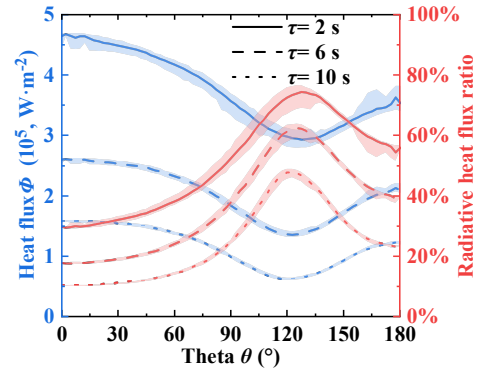

Fig. 5 Distribution of total and radiative heat flux on the slag surface (line: mean value, shadow: value distribution)

3.2 Appraisal of various models and parameters setting

3.2.1 Differences among various dimensional models

Fig. 6 displays the average temperature for planar and axisymmetric 2D models. It's evident that the mean temperature of the axisymmetric model aligns well with the benchmark, whereas the planar model indicates significantly higher results. Calculations of RMSE and MAPE for temperature at different times and angles were also conducted for both models. The results were 235.14 K and 41.30% for the planar model, and 7.67 K and 0.64% for the axisymmetric model. Thus, subsequent cases were computed by the axisymmetric method to balance accuracy and computational cost.
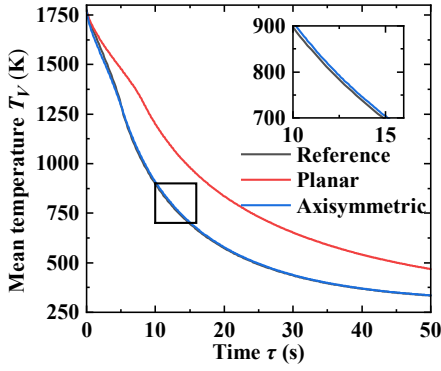
Fig. 6 Comparison of average temperature between reference (3D), planar and axisymmetric 2D models

3.2.2 Error on boundary conditions and width ratio

Fig. 7 depicts the RMSE value of temperature for different boundary conditions and width ratios. All the boundary performs high accuracy under the condition of large WR. However, as the computational domain reduces, RMSE shows significant increases for both zero flux and wall boundary conditions. The RMSE is slightly higher for zero flux with a large domain width ratio, while it is lower for a narrow computational domain. Conversely, the RMSE for the zero-pressure outlet boundary is largely unaffected by the width ratio. However, persistent errors should be noted.
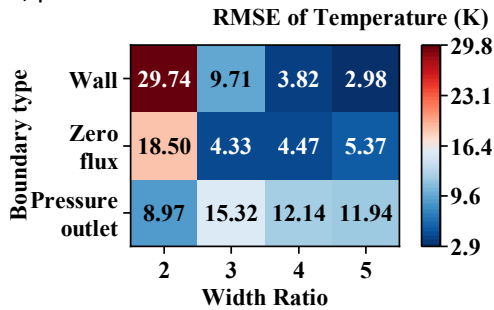

Fig. 7 RMSE of temperature distribution for different boundary types and width ratios

3.2.3 Error on radiation and turbulence

Table 3 lists the RMSE and MAPE of temperature in the models including radiation and turbulence. It's evident that neglecting radiation leads to significant errors, while the effect of the turbulence model is minimal. The variation in error due to different turbulence models is relatively small. However, assuming laminar airflow results in significantly larger errors.

Table 3 RMSE and MAPE of temperature in different factors

Factors	Models	RMSE of Temperature	MAPE of Temperature
Radiation	S2S	7.67 K	0.64%
	None	198.60 K	25.66%
Turbulence	k - ω	7.67 K	0.64%
	k - ε	9.72 K	1.70%
	Laminar	22.21 K	3.75%

4. CONCLUSIONS

In this work, we established a range of cases based on commonly used assumptions and assessed accuracy using an area-weighted angle sampling method. The main conclusions are as follows:

(1) The 2D axisymmetric model can effectively simulate the 3D particle cooling process, as angle-dependent inhomogeneity doesn't manifest significantly in the 3D simulation. However, the 2D planar model will lead to significant errors.

(2) The influence of zero flux and wall boundaries on cooling becomes negligible when the WR exceeds 4. The zero-pressure outlet condition can be cautiously applied for small WR, as the error is not highly sensitive to WR.

(3) Neglecting radiation can result in notable errors in the cooling process, whereas the turbulence model has a small effect.

DECLARATION OF INTEREST STATEMENT

The authors declare that they have no known competing financial interests or personal relationships that could have appeared to influence the work reported in this paper. All authors read and approved the final manuscript.

REFERENCE

[1] Wu J, Tan Y, Li P, Wang H, Zhu X, Liao Q. Centrifugal-Granulation-Assisted thermal energy recovery towards low-carbon blast furnace slag treatment: State of the art and future challenges. Appl Energy 2022;325:119835.

[2] Liu X, Zhu X, Liao Q, Wang H. Theoretic analysis on transient solidification behaviors of a molten blast furnace slag particle. CIESC J 2014;65:285–91.

[3] Sun Y, Shen H, Wang H, Wang X, Zhang Z. Experimental investigation and modeling of cooling processes of high temperature slags. Energy 2014;76:761–7.

[4] Zhu X, Ding B, Wang H, He XY, Tan Y, Liao Q. Numerical study on solidification behaviors of a molten slag droplet in the centrifugal granulation and heat recovery system. Appl Therm Eng 2018;130:1033–43.

[5] Gao J, Feng Y, Feng D, Zhang Z, Zhang X. Solidification with crystallization behavior of molten blast furnace slag particle during the cooling process. Int J Heat Mass Transf 2020;146:118888.

[6] Peng H, Hu Z, Shan X, Ling X, Liu L. Study on the solidification characteristics of molten slag droplets cooled by mixed cooling medium. Appl Therm Eng 2019;149:939–49.

[7] Zhao J, Xu N, Li M, Zhang X, Wu Z, Xiao Z, et al. Investigation on Unsteady Phase-Change Heat Transfer Characteristics of Centrifugal Granulated Particles. Heat Transfer Engineering 2022;43:806–17.

[8] Qiu Y, Zhu X, Wang H, Liao Q. Three-dimensional simulation of solidification and heat transfer for air-cooling molten blast furnace slag droplet. CIESC Journal 2014;65:340–5.

[9] Wang B, Qiu J, Guo Q, Gong Y, Xu J, Yu G. Numerical Simulations of Solidification Characteristics of Molten Slag Droplets in Radiant Syngas Coolers for Entrained-Flow Coal Gasification. ACS Omega 2021;6:20388–97.

[10] Pan Y, Witt PJ, Xie D. CFD simulation of free surface flow and heat transfer of liquid slag on a spinning disc for a novel dry slag granulation process. Progress in Computational Fluid Dynamics 2010;10:292–9.

[11] Tan Y, Wang H, Zhu X, Lv YW, Ding YD, Liao Q. Film fragmentation mode: The most suitable way for centrifugal granulation of large flow rate molten blast slag towards high-efficiency waste heat recovery for industrialization. Appl Energy 2020;276:115454.

[12] Ferreira IL, Spinelli JE, Pires JC, Garcia A. The effect of melt temperature profile on the transient metal/mold heat transfer coefficient during solidification. Materials Science and Engineering: A 2005;408:317–25.